PCCP

PAPER

Cite this: *Phys. Chem. Chem. Phys.*, 2017, **19**, 18416

Two haloid borate crystals with large nonlinear optical response

A. H. Reshak *[a] and S. Auluck[b]

Received 12th April 2017,
Accepted 26th June 2017

DOI: 10.1039/c7cp02364b

rsc.li/pccp

The photophysical properties of the noncentrosymmetric haloid borates $K_3B_6O_{10}X$ (X = Cl or Br) are calculated using density functional theory within the recently modified Becke–Johnson potential. The calculated electronic band structure reveals that the theoretical direct band gaps, 5.21 eV ($K_3B_6O_{10}Cl$) and 4.85 eV ($K_3B_6O_{10}Br$), are in good agreement with the previous calculation for $K_3B_6O_{10}Cl$ (5.16 eV) and experimental data for $K_3B_6O_{10}Br$ (4.86 eV). The calculated absorption coefficients, refractive indices, and birefringence are also in good agreement with the experimental data. The calculated nonzero second harmonic generation (SHG) coefficients, d_{33}, d_{22} (= $-d_{21}$), and d_{15}(= d_{32} = d_{31}), show good agreement with the experimental values. Furthermore, we have obtained the microscopic first hyperpolarizability for the dominant tensor component of the SHG.

1. Introduction

The role of nonlinear optical (NLO) crystals is to generate tunable laser beams covering various optical spectra regions by means of frequency conversion. Currently, the commercially available crystals are capable of harmonic generation in the region from UV to near-IR. Efforts have been made to grow high quality crystals to improve their laser performance in practical applications, and to discover new crystals to extend the spectral coverage into the deep-UV and mid-IR regions. Borate crystals have attracted considerable interest due to their important application in second harmonic generation (SHG).[1–16] Due to the excellent properties of alkaline metal borates and haloid borates, the combination of an alkaline metal and halogen with borate in the same crystal is expected to produce a new class of novel materials with nonlinear optical properties (NLO). Also, it has been reported that combinations of alkaline metal borates and haloid borates with wide transparency and a sufficiently large NLO coefficient are promising materials for efficient SHG from the infrared to ultraviolet spectral ranges.[17,18] The NLO alkaline metal borates and haloid borates have, therefore, played an important role in laser science and technology, and in the search for novel NLO materials for deep-UV applications. It is well known that the crystalline structure of most alkaline metal borates and haloid borates is similar to the perovskite structure. The perovskite structure is considered as a good candidate for a noncentrosymmetric structure type because it is susceptible to distortions which lead to large SHG.[19] It has been reported that the introduction of halogen and alkali metal atoms can widen the transparency range of borates in the UV region.[20–23] As $K_3B_6O_{10}X$ (X = Cl or Br) materials possess a perovskite-like structure, we expect them to have a large SHG response and wide transparency, which makes them promising candidates for deep UV-absorption edge materials. $K_3B_6O_{10}X$ (X = Cl or Br) shows transparency from the deep-UV to middle-IR regions.[24]

There are several reports concerning the synthesis and electronic properties of $K_3B_6O_{10}X$ (X = Cl or Br).[25–29] However, we are not aware of any comprehensive theoretical study of the linear and nonlinear optical properties. Therefore, we were motivated to investigate comprehensively the optical properties using the full-potential method within the recently modified Becke–Johnson potential (mBJ) to treat the exchange correlation potential in order to get an energy gap close to the experimental energy gap. We should emphasize that the reported values of the SHG of $K_3B_6O_{10}Cl$ and $K_3B_6O_{10}Br$ were measured for a powder without taking into account the influence of the packing structural units.[24,27,29–31] Hence, we decided to calculate the SHG of the $K_3B_6O_{10}Cl$ and $K_3B_6O_{10}Br$ crystals, taking into account the influence of the packing structural units using the full-potential method. According to the anionic group theory,[32] the overall SHG response of a crystal is the geometrical superposition of the second-order susceptibilities. Therefore, the packing structural units may also affect the macroscopic SHG coefficients.[33] The large SHG is due to the strong interactions between the structural units.[33] Therefore, the novelty and aim of this work is to present qualitative and quantitative investigations of the SHG values and details of the SHG tensors of $K_3B_6O_{10}Cl$ and $K_3B_6O_{10}Br$ single crystals, taking into account the influence of the packing structural units.

[a] *New Technologies – Research Centre, University of West Bohemia, Univerzitni 8, 306 14 Pilsen, Czech Republic. E-mail: maalidph@yahoo.co.uk; Fax: +420-386 361255; Tel: +420 777729583*

[b] *Council of Scientific and Industrial Research – National Physical Laboratory Dr. K S Krishnan Marg, New Delhi 110012, India*

2. Calculation methodology

The haloid borates $K_3B_6O_{10}X$ (X = Cl or Br) crystallize in the noncentrosymmetric space group *R3m* with three formula units in a unit cell.[24,25] The experimental crystallographic data for $K_3B_6O_{10}X$ (X = Cl or Br)[24,25] are used as input data for the geometrical relaxation of the atoms in the unit cell. The geometrical relaxation is achieved within the Perdew–Burke–Ernzerhof generalized gradient approximation (PBE-GGA).[34] We see that Br (1)/Cl (1) and O(3) atoms occupy the 3a sites, while K(1), B(1), B(2), and O(2) atoms occupy the 9b sites, and O(1) atoms occupy the 18c sites. Fig. 1 shows the crystal structure of the relaxed geometry for $K_3B_6O_{10}Cl$ and $K_3B_6O_{10}Br$. Following Fig. 1, we can see that the K atoms bind with Br or Cl atoms to form a 3D-network. A distorted octahedron (ClK_6 or BrK_6) is formed by the coordination of Cl or Br with six K atoms. Each K atom is surrounded by six O atoms and two Br or Cl atoms in the coordination sphere. The three BO_4 tetrahedra are joined together through corner-sharing of an O atom. The three BO_4 tetrahedra are connected with three BO_3 triangles to form a compact hexaborate unit (B_6O_{13}) which inserts in the K-Cl or K-Br network. Fig. 1(e and f) show that the charge localizes mainly between B and the neighboring O atoms, indicating a strong covalent bonding which defines the structure of the borate units [BO_3] and [BO_4].

Using the obtained relaxed geometry, the linear and nonlinear optical properties and the first hyperpolarizability are calculated using the all-electrons full-potential linear augmented plane wave (FPLAPW+lo) method as embodied in the Wien2k code,[35] utilizing the modified Becke–Johnson potential (mBJ) to treat the exchange correlation.[36] The mBJ is a local approximation of an atomic "exact-exchange" potential and a screening term which allows the calculation of band gaps with accuracy similar to the expensive GW calculations.[36] We would like to mention here that in our previous work[37–42] we have calculated the linear and nonlinear optical susceptibilities using the FPLAPW method within mBJ on several systems whose linear and nonlinear optical susceptibilities are known experimentally. In these calculations, we found very good agreement with the experimental data. Thus, we believe that our calculations reported in this article will produce very accurate and reliable results.

For $K_3B_6O_{10}Cl$ and $K_3B_6O_{10}Br$, the muffin-tin radii (R_{MT}) of the K, B, O, Cl, and Br atoms were chosen in such a way that the spheres did not overlap. The values of R_{MT} are taken to be 2.46 a.u. (K), 2.5 a.u. (Cl), 1.13 a.u. (B), and 1.31 a.u. (O) for $K_3B_6O_{10}Cl$ and 2.41 a.u. (K), 2.5 a.u. (Br), 1.18 a.u. (B), and 1.37 a.u. (O) for $K_3B_6O_{10}Br$. To achieve the total energy convergence, the basis functions in the interstitial region (IR) were expanded up to $R_{MT} \times K_{max} = 7.0$. The $R_{MT} \times K_{max}$ determines the matrix size (convergence), where K_{max} is the plane wave cut-off, and R_{MT} is the smallest of all atomic sphere radii. The maximum value of $\boldsymbol{l}$ was taken as $\boldsymbol{l}_{max} = 10$, where $\boldsymbol{l}_{max}$ is the maximum value of the angular momentum for the expansion in spherical harmonics of the product of two orbitals and the generated potential inside the atomic spheres. The charge density is Fourier expanded up to $G_{max} = 12$ (a.u.)$^{-1}$, where G_{max} is the magnitude of the largest vector G in the Fourier expansion of the product of two orbitals and the generated potential in the interstitial region. Self-consistency is obtained using 400 $\vec{k}$ points in the irreducible Brillouin zone (IBZ). The self-consistent calculations are converged when the total energy of the system is stable within 0.00001 Ry. The linear and nonlinear optical properties and the microscopic first hyperpolarizability calculations are performed with 1834 $\vec{k}$ points in the IBZ. The linear optical properties are calculated using the optical code implemented in the WIEN2k package.[35] For more details about FPLAPW, we refer the reader to well-known ref. 43 and 44. The nonlinear optical properties are calculated using the NLO code[45] which is compatible with the WIEN2k package.

3. Results and discussion

3.1. Salient features of the electronic structure

To understand the origin of the linear optical properties and the source of the large SHG of $K_3B_6O_{10}Cl$ and $K_3B_6O_{10}Br$, the electronic band structure is calculated and presented in Fig. 2(a) and (b) along with the optical transitions depicted on the generic band structure. The calculated electronic band structure reveals the nature of the band gaps of $K_3B_6O_{10}Cl$ and $K_3B_6O_{10}Br$. It was found that the valence band maximum (VBM) and the conduction band minimum (CBM) are located at the center of the Brillouin zone (*i.e.* direct band gap). The VBM consists of O-2p and Cl-3p (Br-4p) states, whereas the CBM is mainly composed of B-2p states of the B1 atom. The calculated energy band gaps are 5.21 eV ($K_3B_6O_{10}Cl$) and 4.85 eV ($K_3B_6O_{10}Br$), which are in good agreement with the previous calculation for $K_3B_6O_{10}Cl$ (5.16 eV)[25] and experimental data for $K_3B_6O_{10}Br$ (4.86 eV).[26] A material with such an energy band gap value is expected to possess a high laser damage threshold.[46,47] It was noticed that replacing Cl by Br reduces the energy band gap by 0.36 eV, which has a significant influence on the linear and nonlinear optical properties. We should emphasize that the nonlinear optical properties are much more sensitive to the value of the energy band gap compared to the linear optical properties. The reduction in the energy band gap could be attributed to the fact that the atomic radii of Br (115 pm) are greater than those of Cl (100 pm), which influences the bond length and pushes the conduction band towards the Fermi level (E_F). Analyzing the electronic distribution is an important factor to investigate the origin of optical properties.[48,49] Deep insight into the electronic structure can be obtained from analyzing the electron cloud of the BO_3 and BO_4 groups (Fig. 1e and f). The electron cloud of the BO_3 groups exhibits a planar shape with conjugated electron orbitals. Fig. 1e shows a high electron density configuration and strong anisotropy for B–O groups, resulting in contributions to the optical anisotropy of the BO_3 groups.

3.2. Complex first-order linear optical dispersion and birefringence

The imaginary part of the dielectric function $\varepsilon_2^{\perp}(\omega)$ and $\varepsilon_2^{\parallel}(\omega)$ of $K_3B_6O_{10}Cl$ and $K_3B_6O_{10}Br$ shown in Fig. 3 are calculated from the momentum matrix elements between the occupied and

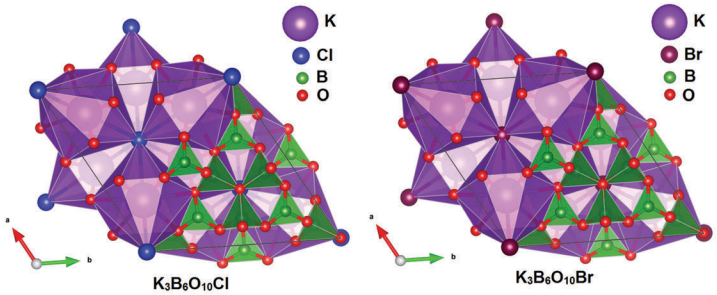

(a) Three building blocks of $K_3B_6O_{10}Cl$: BO_3 triangle, BO_4 tetrahedron and ClK_6 octahedron

(b) Three building blocks of $K_3B_6O_{10}Br$: BO_3 triangle, BO_4 tetrahedron and BrK_6 octahedron

Each K atom is surrounded by six O atoms and two Br or Cl atoms in the coordination sphere.

BO_3 triangles BO_4 tetrahedra BO_3 triangles BO_4 tetrahedra

(c)

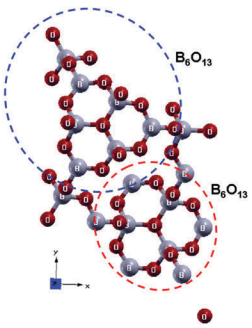

(d) Here we have removed the K and Cl (Br) atoms to visualize the structures of the BO_3, BO_4 and B_6O_{13}. The three BO_4 tetrahedra are joined together through corner-sharing of an O atom, also the BO_4 tetrahedra are connected with three BO_3 triangles to form B_6O_{13} the compact hexaborate unit in $K_3B_6O_{10}Cl$ and $K_3B_6O_{10}Br$.

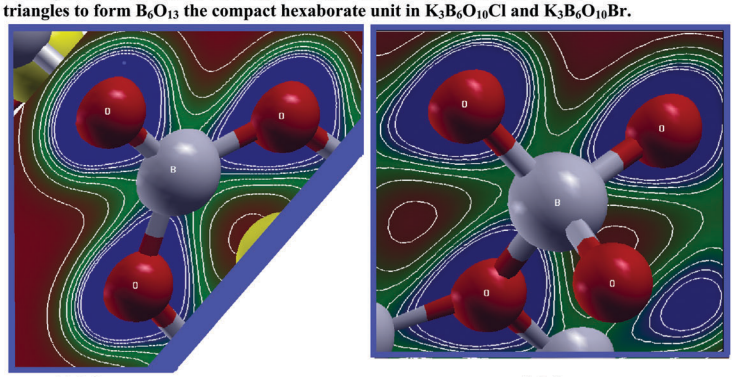

(e) BO_3 **(f) BO_4**

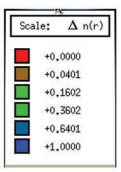

(g)

These B–O units possess strong electron cloud overlap.

Fig. 1 (a and b) The crystal structure of the relaxed geometry of the noncentrosymmetric haloid borate $K_3B_6O_{10}X$ (X = Cl or Br) with three formulae per unit cell. It is clear that the Br(1)/Cl(1) and O(3) atoms occupy the site 3a, while K(1), B(1), B(2), and O(2) atoms occupy the 9b position, and O(1) atoms occupy the site 18c. We can see that the K atoms bind with Br or Cl atoms to form a 3D-network. Each Br or Cl atom is coordinated by six K atoms (KCl_6 or BrK_6) in distorted octahedra. In $K_3B_6O_{10}Cl$ and $K_3B_6O_{10}Br$ each K atom is surrounded by six O atoms and two Br or Cl atoms in the coordination sphere, the three BO_4 tetrahedra are joined together through corner-sharing of an O atom, and the BO_4 tetrahedra are connected with three BO_3 triangles to form B_6O_{13} (compact hexaborate unit) which inserts into a K-Cl or K-Br network; (c) BO_3 triangles and BO_4 tetrahedra; (d) here we have removed the K and Cl (Br) atoms to visualize the structures of the BO_3, BO_4, and B_6O_{13}. (e and f) The borate units [BO_3] and [BO_4] which form B_6O_{13} (compact hexaborate unit). These B–O units possess strong electron cloud overlap. The high electron density configuration and strong anisotropy of B–O groups indicate the main contribution of BO_3 and BO_4 groups to the optical anisotropy; (g) thermo-scale.

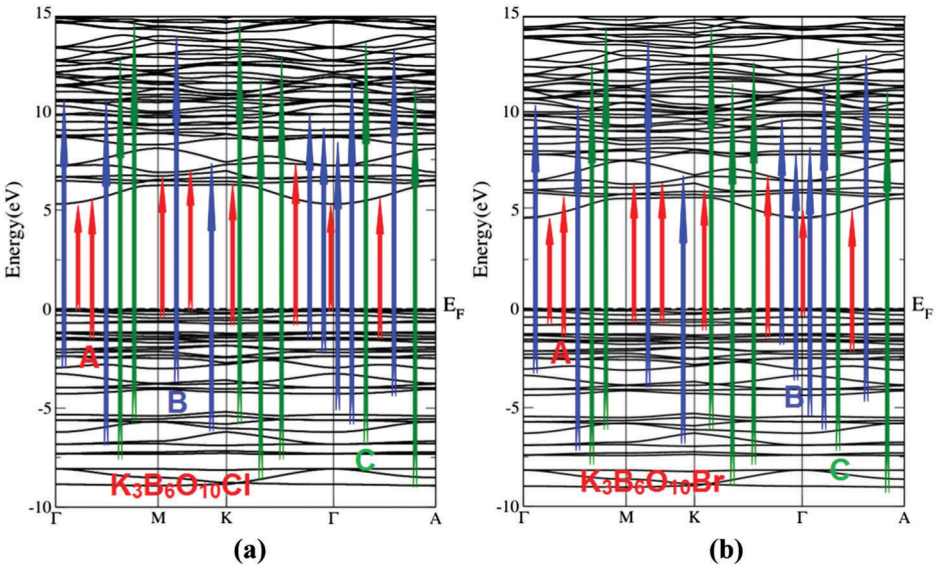

Fig. 2 The optical transitions depicted on a generic band structure of the noncentrosymmetric haloid borate $K_3B_6O_{10}X$ (X = Cl or Br).

unoccupied electronic states. The real part of the dielectric function $\varepsilon_1^{\perp}(\omega)$ and $\varepsilon_1^{\parallel}(\omega)$ can be evaluated from $\varepsilon_2^{\perp}(\omega)$ and $\varepsilon_2^{\parallel}(\omega)$ by using the Kramer–Kronig relation.[50] The diagonal elements of the calculated optical dielectric tensor ε^{∞} of $K_3B_6O_{10}Cl$ ($K_3B_6O_{10}Br$) are listed in Table 1. The mBJ results show better agreement with the experimental data. Due to substitution of Cl by Br and the reduction in the energy band gap, there is a significant influence on the optical transitions and hence the spectral features of the imaginary and real parts of the dielectric function. The BO_3 and BO_4 groups are the main building blocks of the borate crystals. Therefore, the high electron density configuration and strong anisotropy of the B–O groups are the main contributors to the optical anisotropy of the BO_3 groups. As $K_3B_6O_{10}Br$ possesses a smaller energy band gap than $K_3B_6O_{10}Cl$, we expect larger values for $\varepsilon_1^{\perp}(0)$ and $\varepsilon_1^{\parallel}(0)$. This could be explained on the basis of the Penn model.[51] Penn proposed a relation between $\varepsilon(0)$ and E_g, $\varepsilon(0) \approx 1 + (\hbar\omega_P/E_g)^2$. E_g is an averaged energy gap which could be related to the real energy gap. Hence, a larger E_g yields a smaller $\varepsilon(0)$. There are other features in the optical spectrum, such as plasmon oscillations, which are associated with inter-band transitions. The plasmon maximum is usually the most intense feature in the spectrum and this is at an energy level where $\varepsilon_1^{\perp}(\omega)$ and $\varepsilon_1^{\parallel}(\omega)$ cross zero. The plasma frequencies ($\omega_p^{\perp}$ and $\omega_p^{\parallel}$) of $K_3B_6O_{10}Cl$ and $K_3B_6O_{10}Br$ are presented in Table 1.

The other important feature is the uniaxial anisotropy ($\delta\varepsilon = (\varepsilon_0^{\parallel} - \varepsilon_0^{\perp})/\varepsilon_0^{\text{total}}$), which can be calculated from $\varepsilon_1^{\perp}(0)$ and $\varepsilon_1^{\parallel}(0)$. It was found that $K_3B_6O_{10}Cl$ and $K_3B_6O_{10}Br$ exhibit negative $\delta\varepsilon$, as shown in Table 1. Therefore, $K_3B_6O_{10}Cl$ and $K_3B_6O_{10}Br$ are negative uniaxial optical crystals ($n_0 > n_e$), which agrees well with the experimental findings.[26,27]

Furthermore, with the aid of the imaginary and real parts of the dielectric function, we obtained the imaginary and real parts of the optical conductivities of $K_3B_6O_{10}Cl$ and $K_3B_6O_{10}Br$, and this is shown in Fig. 3c and d. It is clear that the imaginary parts of the optical conductivity between 0.0 and the values of $\omega_p^{\perp}$ and $\omega_p^{\parallel}$ exhibit overturned features of $\varepsilon_2^{\perp}(\omega)$ and $\varepsilon_2^{\parallel}(\omega)$, whereas the real parts show features similar to those of $\varepsilon_2^{\perp}(\omega)$ and $\varepsilon_2^{\parallel}(\omega)$.

Fig. 3e and f represent the loss function peaks of $K_3B_6O_{10}Cl$ and $K_3B_6O_{10}Br$. The loss function peaks were initiated at the values of the plasma frequencies $\omega_p^{\perp}$ and $\omega_p^{\parallel}$ and represent the negative parts of $\varepsilon_1^{\perp}(\omega)$ and $\varepsilon_1^{\parallel}(\omega)$. The calculated optical reflectivities of $K_3B_6O_{10}Cl$ and $K_3B_6O_{10}Br$ are shown in Fig. 3g and h. It is clear that in the low energy region both compounds show low reflectivity. The main reflectivity minimum is situated at around 12.0 eV, confirming the occurrence of a collective plasmon resonance in concordance with our observation in Fig. 3a and b. At higher energies, the region between 12.5 and 14.0 eV reflectivity shows a lossless region.

The frequency-dependent absorption coefficients of $K_3B_6O_{10}Cl$ and $K_3B_6O_{10}Br$ (Fig. 3i and j) can be divided into four regions. These are the low absorption region, high absorption region, lossless region, and high transparent region. The calculated fundamental absorption edges of $I^{\perp}(\omega)$ and $I^{\parallel}(\omega)$ for $K_3B_6O_{10}Cl$ ($K_3B_6O_{10}Br$) occur at 5.15 eV (4.85 eV), which is in good agreement with the experimental data.[25,26] The optical band gap can be obtained by noting that the square of the absorption coefficient $I(\omega)$ is linear with energy (E) for direct optical transitions in the absorption edge region, whereas the square root of $I(\omega)$ is linear with E for indirect optical transitions.[52,53] As the calculated electronic band structure of $K_3B_6O_{10}Cl$ and $K_3B_6O_{10}Br$ confirms the direct nature of the band gap, the data plots of $[I(\omega)]^2$ *versus* E are shown in the inset of Fig. 3i and j. It is clearly shown that $[I(\omega)]^2$ *versus* E is linear in the absorption edge region. Following Fig. 3i and j, we can conclude that the absorption edges of $K_3B_6O_{10}Cl$ and $K_3B_6O_{10}Br$ occur at λ = 237.9 nm and λ = 255.6 nm, and the optical band gaps are estimated to be 5.21 eV and 4.85 eV for $K_3B_6O_{10}Cl$ and $K_3B_6O_{10}Br$, respectively.

The calculated refractive indices of $K_3B_6O_{10}Cl$ and $K_3B_6O_{10}Br$ are shown in Fig. 3k and l. Following Fig. 3k and l, the values of the birefringence ($\Delta n(\omega) = n_e(\omega) - n_o(\omega)$) can be obtained, where $n_e(\omega)$ is the index of refraction for an electric field oriented along the *c*-axis, *i.e.* $n^{\parallel}(\omega)$, and $n_o(\omega)$ is the index of refraction for an electric field perpendicular to the *c*-axis, *i.e.* $n^{\perp}(\omega)$. This is shown in Fig. 3m. The calculated values of $n^{\perp}(\omega)$, $n^{\parallel}(\omega)$, $\Delta n(0)$, and $\Delta n(\omega)$ at λ = 1064 nm are given in Table 1. Our calculated refractive indices are in concordance with measured ones and previous calculations.[54,55] Zhang *et al.*[27] reported that the measured birefringence value of $K_3B_6O_{10}Br$ is about 0.046–0.049 between 404.7 nm and 694.3 nm. The birefringence of $K_3B_6O_{10}Br$ (Δn = 0.046, 1064 nm) is comparable to that of LiB_3O_5 (LBO), CsB_3O_5 (CBO) and $BaAlBO_3F_2$ (BABF) crystals,[56–58] which indicates that $K_3B_6O_{10}Br$ may have good phase-matching properties.[26] Following Table 1 and the experimental measurements,[26,27,56–58] we can

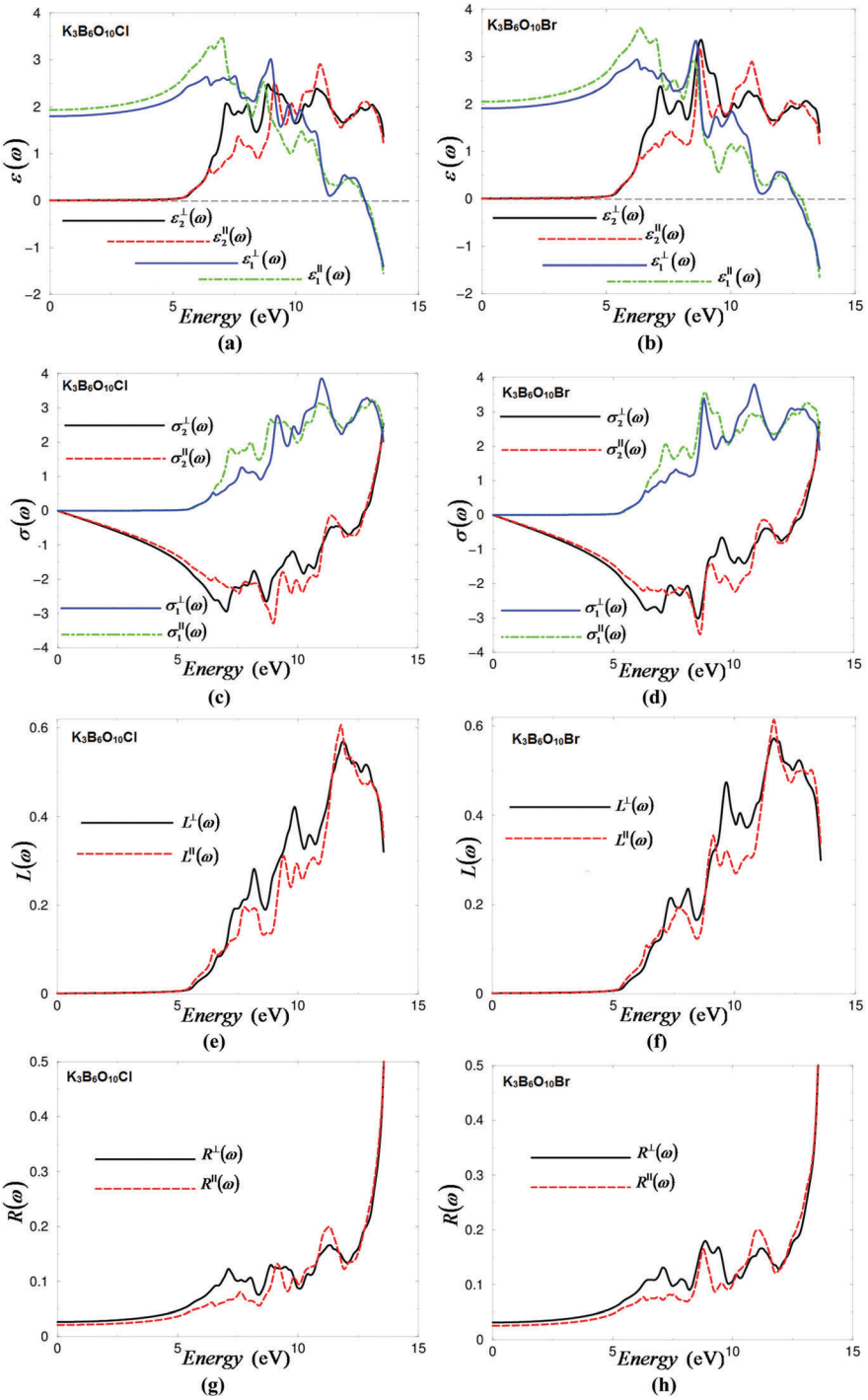

Fig. 3 (continued)

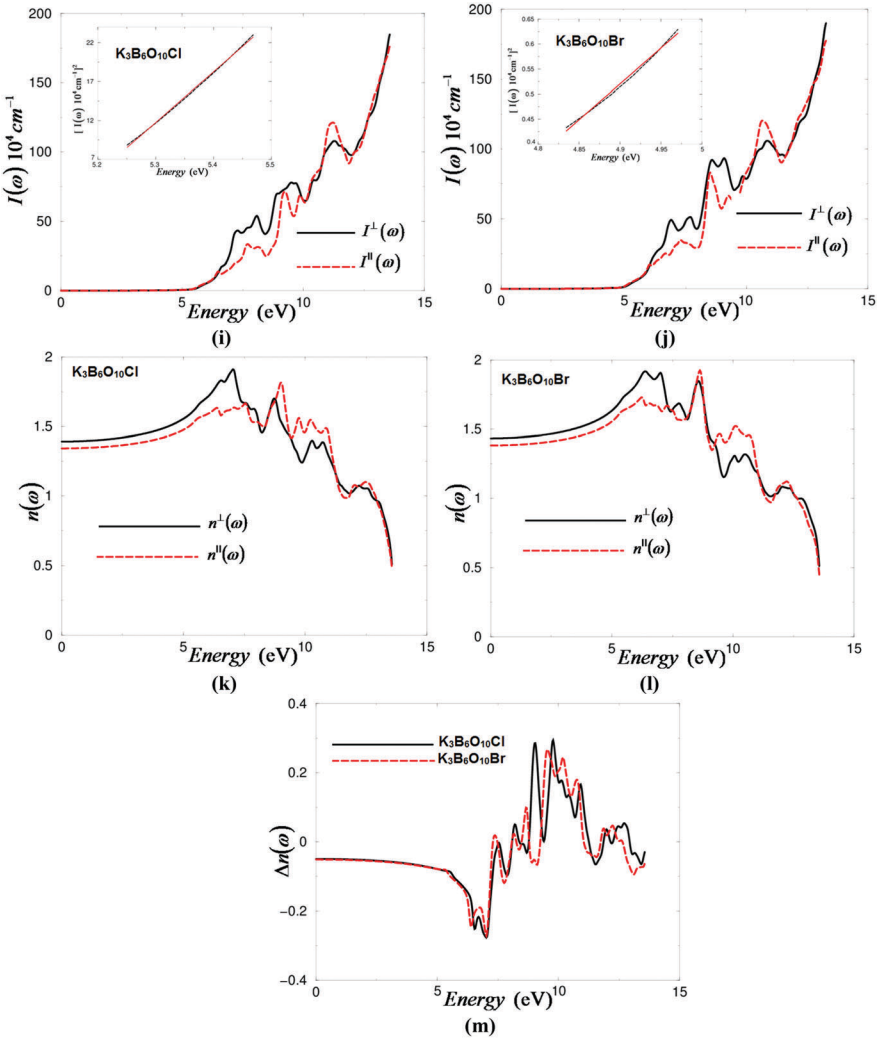

Fig. 3 (a and b) Calculated $\varepsilon_2^{xx}(\omega)$ (black solid curve), $\varepsilon_2^{yy}(\omega)$ (red long dashed curve) and $\varepsilon_2^{zz}(\omega)$ (green dotted dashed curve) along with calculated $\varepsilon_1^{xx}(\omega)$ (blue solid curve), $\varepsilon_1^{yy}(\omega)$ (brown dashed curve) and $\varepsilon_1^{zz}(\omega)$ (violet solid curve) for $K_3B_6O_{10}X$ (X = Cl or Br); (c and d) calculated $\sigma_2^{xx}(\omega)$ (black solid curve), $\sigma_2^{yy}(\omega)$ (red dashed curve) and $\sigma_2^{zz}(\omega)$ (green dotted dashed curve) along with calculated $\sigma_1^{xx}(\omega)$ (blue solid curve), $\sigma_1^{yy}(\omega)$ (red brown dashed curve) and $\sigma_1^{zz}(\omega)$ (violet solid curve) for $K_3B_6O_{10}X$ (X = Cl or Br); (e and f) calculated loss function $L^{xx}(\omega)$ (black solid curve), $L^{yy}(\omega)$ (red dashed curve) and $L^{zz}(\omega)$ (blue dotted dashed curve) spectrum for $K_3B_6O_{10}X$ (X = Cl or Br); (g and h) calculated $R^{xx}(\omega)$ (black solid curve), $R^{yy}(\omega)$ (red dashed curve), and $R^{zz}(\omega)$ (blue dotted dashed curve) for $K_3B_6O_{10}X$ (X = Cl or Br); (i and j) calculated absorption coefficient $I^{xx}(\omega)$ (black solid curve), $I^{yy}(\omega)$ (red dashed curve) and $I^{zz}(\omega)$ (blue dotted dashed curve) spectrum for $K_3B_6O_{10}X$ (X = Cl or Br), the inset show the data plots of the $[I(\omega)]^2$ *versus* E. The absorption coefficient in 10^4 cm^{-1}; (k and l) calculated refractive indices $n^{xx}(\omega)$ (black solid curve), $n^{yy}(\omega)$ (red dashed curve) and $n^{zz}(\omega)$ (blue dotted dashed curve) spectrum for $K_3B_6O_{10}X$ (X = Cl or Br); (m) calculated birefringence $\Delta n(\omega)$.

conclude that $K_3B_6O_{10}Cl$ and $K_3B_6O_{10}Br$ exhibit relatively large birefringence. Based on the discussion of Bian *et al.*[59] regarding the electron cloud of BO_3 anionic groups which exhibit a planar shape with conjugated electron orbitals, which also make the BO_3 anionic groups the main source of the large birefringence in Pb_2BO_3F, we expect BO_3 to be the source of the large birefringence in $K_3B_6O_{10}Cl$ and $K_3B_6O_{10}Br$. It is well known that the birefringence determines partly whether a material has interesting NLO properties.[59] The calculated linear optical properties show considerable anisotropy between the parallel and the perpendicular components, which favors an important quantity in SHG and optical parametric oscillation (OPO) or amplification (OPA) due to better fulfillment of the phase-matching conditions determined by birefringence.

Table 1 The calculated energy band gaps of $K_3B_6O_{10}Cl$ and $K_3B_6O_{10}Br$ in comparison with the experimental data[25] and the previous calculation,[26] $\varepsilon_1^{\perp}(0)$, $\varepsilon_1^{\parallel}(0)$, $\delta\varepsilon$, $\omega_p^{\perp}(\omega)$, $\omega_p^{\parallel}(\omega)$, $n^{\perp}(0)$, $n^{\parallel}(0)$, $\Delta n(0)$ and $\Delta n(\omega)$. In this work the parameters are calculated within mBJ

	$K_3B_6O_{10}Cl$	$K_3B_6O_{10}Br$
E_g (eV)	5.21, 5.16[a]	4.85, 4.86[b]
$\varepsilon_1^{\perp}(0)$	1.937	2.054, 2.3[c]
$\varepsilon_1^{\parallel}(0)$	1.802	1.910, 2.8[c]
$\delta\varepsilon$	−0.0361	−0.0363
$\omega_p^{\perp}(\omega)$	12.802	12.857
$\omega_p^{\parallel}(\omega)$	12.830	12.666
$n^{\perp}(0)$	1.391	1.433
$n^{\parallel}(0)$	1.342	1.382
$\Delta n(0)$	−0.049	−0.051
$\Delta n(\omega)$ at λ = 1064 nm	−0.045	−0.044

[a] Ref. 25. [b] Ref. 26. [c] Ref. 28 using Quantum Espresso package within LDA.

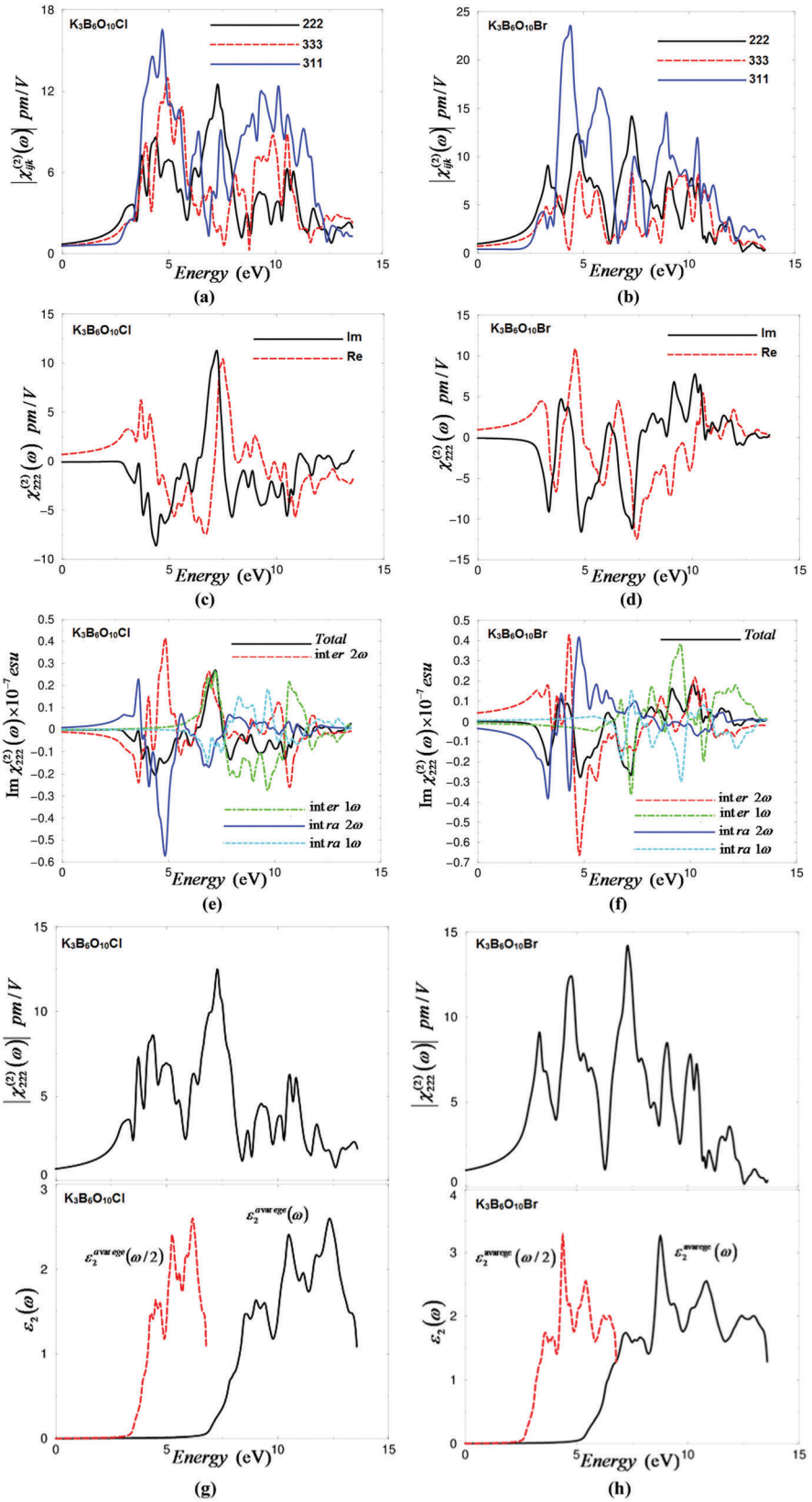

Fig. 4 (a and b) Calculated $|\chi^{(2)}_{ijk}(\omega)|$ for the three tensor components of the noncentrosymmetric haloid borate $K_3B_6O_{10}X$ (X = Cl or Br); (c and d) calculated imaginary $\chi^{(2)}_{222}(\omega)$ (black solid curve) and real $\chi^{(2)}_{222}(\omega)$ (red dashed curve) spectra for $K_3B_6O_{10}X$ (X = Cl or Br); (e and f) calculated total $\mathrm{Im}\chi^{(2)}_{222}(\omega)$ spectrum (black solid curve) along with the intra $(2\omega)/(1\omega)$ (blue solid curve)/(cyan dashed dotted curve) and inter $(2\omega)/(1\omega)$ (red long dashed curve)/(green dotted curve)-band contributions for $K_3B_6O_{10}X$ (X = Cl or Br), here all $\mathrm{Im}\chi^{(2)}_{222}(\omega)$ are multiplied by 10^{-7}, in esu units; (g and h) – upper panel – calculated $|\chi^{(2)}_{222}(\omega)|$ (black solid curve); – lower panel – calculated $\varepsilon_2^{xx}(\omega)$ (black solid curve); calculated $\varepsilon_2^{xx}(\omega/2)$ (red dashed curve) for $K_3B_6O_{10}X$ (X = Cl or Br).

3.3. Complex second-order nonlinear optical dispersion

$K_3B_6O_{10}Cl$ and $K_3B_6O_{10}Br$ belong to the point group $3m$. Using Kleinman symmetry,[60] there are three independent nonzero SHG coefficients: these are d_{33}, $d_{22} = -d_{21}$, and $d_{15} = d_{32} = d_{31}$, respectively. The trigonal BO_3 anionic group possessing a conjugated π orbital is one of the most active NLO clusters in borate crystals. The unit cell of $K_3B_6O_{10}X$ (X = Cl or Br) contains BO_3 triangles, BO_4 tetrahedra, and KO_6Br_2 or KO_6Cl_2 polyhedra. The major component of SHG in $K_3B_6O_{10}X$ (X = Cl or Br) comes mainly from the BO_3 triangles and to a large degree from the polarization of the ClK_6 or BrK_6 octahedra, whereas KO_6Br_2 or KO_6Cl_2 polyhedra and BO_4 tetrahedra contribute less.[61] The B atom has two types of hybridized orbitals, the planar sp^2 and the three-dimensional sp^3, to coordinate three or four O atoms forming BO_3^{3-}, BO_3^{4-} or BO_4^{5-} clusters. Further, these clusters can comprise several different typical B_xO_y groups, and therefore various types of borate crystals can be constructed based on these infrastructures. This is a very attractive phenomenon discovered in inorganic borate crystals. Therefore, it is very interesting to study the influence of BO_3^{3-}, BO_3^{4-} or BO_4^{5-} clusters on the second-order nonlinear optical response of various types of borate crystals, so as to get some useful information while searching for efficient nonlinear optical materials.[62]

Fig. 4a and b show the absolute values of $|\chi^{(2)}_{222}(\omega)|$, $|\chi^{(2)}_{311}(\omega)|$ and $|\chi^{(2)}_{333}(\omega)|$ for $K_3B_6O_{10}Cl$ and $K_3B_6O_{10}Br$. We note that there is considerable anisotropy between the three tensor components. A definite enhancement in the anisotropy going from the linear optical properties to the nonlinear optical properties is evident. It was found that $|\chi^{(2)}_{222}(\omega)|$ is the dominant tensor component for $K_3B_6O_{10}Cl$ and $K_3B_6O_{10}Br$ at the static limit and at λ = 1064 nm. In Tables 2 and 3 we give the values of all tensor components at the static limit and at λ = 1064 nm. The obtained values of d_{22}, d_{31}, and d_{33} for $K_3B_6O_{10}Cl$ and $K_3B_6O_{10}Br$ at λ = 1064 nm show good agreement with the reported measured values.[26,29] It has been reported that $K_3B_6O_{10}Cl$ and $K_3B_6O_{10}Br$ show a relatively large effective SHG coefficient of about three times that of KDP.[26,27,29,31] It was found that $K_3B_6O_{10}Br$ (E_g = 4.85 eV) gives a larger SHG than $K_3B_6O_{10}Cl$ (E_g = 5.15 eV). A smaller energy gap gives better SHG performance but limits the transmittance in the UV region. Thus, NLO materials used in the UV region are governed by a delicate balance between the SHG response and band gap.[63]

The imaginary and real parts of the dominant tensor component for $K_3B_6O_{10}Cl$ and $K_3B_6O_{10}Br$ are shown in Fig. 4c and d. The 2ω terms start oscillating at energy which is about half the energy gap and the ω terms start to oscillate at the value of the energy gap, while the tail of the imaginary part originates from the ω terms only.

The imaginary and real parts are further separated into $2\omega/\omega$ inter-/intra-band contributions, which oscillate around zero and exhibit considerable anisotropy, as shown in Fig. 4e and f. The spectral features of the dominant tensor component $|\chi^{(2)}_{222}(\omega)|$ for $K_3B_6O_{10}Cl$ and $K_3B_6O_{10}Br$ are analyzed in order to understand the origin of the SHG. To achieve this, we have associated the spectral structures of the dominant tensor component with the absorptive part of the corresponding dielectric function $\varepsilon_2(\omega)$ as a function of both $\omega/2$ and ω as shown in Fig. 4g and h. For simplicity, we proposed dividing the spectral structures in $|\chi^{(2)}_{222}(\omega)|$, $\varepsilon_2(\omega)$ and $\varepsilon_2(\omega/2)$ into three spectral regions. The spectral region which is confined between the half value and the fundamental value of the energy band gap is mainly formed by the 2ω resonance, which is associated with the first spectral structure of $\varepsilon_2(\omega/2)$. The second spectral region from the fundamental value of the energy band gap up to 7.5 eV is associated with interference between 2ω and ω resonances, which is associated with the second part of the spectral structure of $\varepsilon_2(\omega/2)$ and the first part of the spectral structure of $\varepsilon_2(\omega)$. It is clear that in this region the ω terms start to oscillate and contribute to the spectral structure of $|\chi^{(2)}_{222}(\omega)|$ in addition to 2ω terms. The third spectral structure from 7.5 eV to 13.5 eV is mainly due to ω resonance which is associated with the second spectral structure in $\varepsilon_2(\omega)$.

3.4. Microscopic first hyperpolarizability

The microscopic first hyperpolarizability, β_{ijk},[64] the vector component along the dipole moment direction, at the static limit and at λ = 1064 nm, can be obtained from the calculated $|\chi^{(2)}_{ijk}(\omega)|$. The β_{ijk} term cumulatively yields a bulk observable second-order susceptibility term, which in turn is responsible for the strong SHG response.[65] We should emphasize that going from Cl to Br a band gap reduction occurs, hence changing the SHG value; therefore, we expected that $K_3B_6O_{10}Cl$ and $K_3B_6O_{10}Br$ possess different β_{ijk} terms. The values of β_{ijk} for $K_3B_6O_{10}Cl$ and $K_3B_6O_{10}Br$ are calculated for the dominant component at the static limit and at λ = 1064 nm, as listed in Tables 2 and 3.

Table 2 Calculated $|\chi^{(2)}_{ijk}(\omega)|$ and β_{ijk} of $K_3B_6O_{10}Cl$, in pm V^{-1} at the static limit and at λ = 1064 nm, where 1 pm V^{-1} = 2.387 × 10^{-9} esu

$K_3B_6O_{10}Cl$					
Tensor components	$\chi^{(2)}_{ijk}(0)$	$d_{ijk} = 0.5\chi^{(2)}_{ijk}(\omega)$ at static limit	$\chi^{(2)}_{ijk}(\omega)$ at λ = 1064 nm	$d_{ijk} = 0.5\chi^{(2)}_{ijk}(\omega)$ at λ = 1064 nm	d_{ijk} (previous calculations) at λ = 1064 nm
$\lvert\chi^{(2)}_{222}(\omega)\rvert$	0.701	d_{22} = 0.350	0.981	d_{22} = 0.490	d_{22} = 2.58[a]
$\lvert\chi^{(2)}_{311}(\omega)\rvert$	0.568	d_{31} = 0.284	0.638	d_{31} = 0.319	Not available
$\lvert\chi^{(2)}_{333}(\omega)\rvert$	0.569	d_{33} = 0.285	0.755	d_{33} = 0.378	d_{33} = 0.03[a]
β_{222}	0.593 × 10^{-30} esu		0.828 × 10^{-30} esu		

[a] Ref. 53 theoretical (under pressure).

Table 3 Calculated $|\chi^{(2)}_{ijk}(\omega)|$ and β_{ijk} of $K_3B_6O_{10}Br$, in pm V^{-1} at the static limit and at λ = 1064 nm, where 1 pm V^{-1} = 2.387 × 10^{-9} esu

$K_3B_6O_{10}Br$					
Tensor components	$\chi^{(2)}_{ijk}(0)$	$d_{ijk} = 0.5\chi^{(2)}_{ijk}(\omega)$ at static limit	$\chi^{(2)}_{ijk}(\omega)$ at λ = 1064 nm	$d_{ijk} = 0.5\chi^{(2)}_{ijk}(\omega)$ λ = 1064 nm	d_{ijk} (Exp.) at λ = 1064 nm
$\lvert\chi^{(2)}_{222}(\omega)\rvert$	0.978	d_{22} = 0.489	1.4	d_{22} = 1.2	$d_{22} = 1.23 \pm 0.01^a$ $d_{22} = 0.83^b$ $d_{22} = 1.5645^c$
$\lvert\chi^{(2)}_{311}(\omega)\rvert$	0.413	d_{31} = 0.207	0.423	d_{31} = 0.212	$d_{31} = -0.2756^c$
$\lvert\chi^{(2)}_{333}(\omega)\rvert$	0.729	d_{33} = 0.365	1.0	d_{33} = 0.5	$d_{33} = 0.43 \pm 0.01^a$ $d_{33} = 0.51^b$ $d_{33} = -1.1564^c$
β_{222}	0.836 × 10^{-30} esu		1.175 × 10^{-30} esu		

[a] Ref. 52. [b] Ref. 26 (experimental data). [c] Ref. 26 (calculated).

4. Conclusions

Based on the calculated electronic band structures, the linear and nonlinear optical properties of the noncentrosymmetric haloid borates $K_3B_6O_{10}X$ (X = Cl or Br) are calculated and discussed in detail. The all-electron full-potential method within the recently modified Becke–Johnson potential is used to calculate the band structures and the linear and nonlinear optical properties. The calculated electronic band structure reveals that the theoretical direct band gaps 5.21 eV ($K_3B_6O_{10}Cl$) and 4.85 eV ($K_3B_6O_{10}Br$) are in good agreement with the previous calculation for $K_3B_6O_{10}Cl$ (5.16 eV) and experimental data for $K_3B_6O_{10}Br$ (4.86 eV). The energy gap value confirms that $K_3B_6O_{10}X$ (X = Cl or Br) exhibits an exceptional laser damage threshold. The calculated absorption coefficients, refractive indices, and birefringence are in concordance with measured values. The three calculated independent nonzero second harmonic generation (SHG) coefficients, d_{33}, $d_{22} = -d_{21}$, and $d_{15} = d_{32} = d_{31}$, also show good agreement with the measured values. Furthermore, we have obtained the microscopic first hyperpolarizability for the dominant tensor component of the SHG.

Acknowledgements

The result was developed within the CENTEM project, reg. no. CZ.1.05/2.1.00/03.0088, co-funded by the ERDF as part of the Ministry of Education, Youth and Sports OP RDI program and, in the follow-up sustainability stage, supported through CENTEM PLUS (LO1402) by financial means from the Ministry of Education, Youth and Sports under the "National Sustainability Program I. Computational resources were provided by MetaCentrum (LM2010005) and CERIT-SC (CZ.1.05/3.2.00/08.0144) infrastructures. SA would like to acknowledge the use of the computing facilities at the Physics Department of Indian Institute of Technology in Kanpur (IITK), the Intra-University Accelerator Centre (IUAC) in New Delhi, the Institute of Mathematical Sciences (IMSC) in Chennai, and the Council of Scientific and Industrial Research Fourth Paradigm Institute (CSIR-4PI) at Bengaluru.

References

1 P. Becker, *Adv. Mater.*, 1998, **10**, 979–992.
2 T. Sasaki, Y. Mori, M. Yoshimura, Y. K. Yap and T. Kamimura, *Mater. Sci. Eng., R*, 2000, **30**, 1–54.
3 P. S. Halasyamani and K. R. Poeppelmeier, *Chem. Mater.*, 1998, **10**, 2753–2769.
4 C. T. Chen, Z. S. Lin and Z. Z. Wang, *Appl. Phys. B: Lasers Opt.*, 2005, **80**, 1–25; C. T. Chen, Y. B. Wang, B. C. Wu, K. C. Wu, W. L. Zeng and L. H. Yu, *Nature*, 1995, **373**, 322–324.
5 E. L. Belokoneva, *Crystallogr. Rev.*, 2005, **11**, 151–198.
6 S. L. Pan, J. P. Smit, B. Watkins, M. R. Marvel, C. L. Stern and K. R. Poeppelmeier, *J. Am. Chem. Soc.*, 2006, **128**, 11631–11634.
7 E. O. Chi, K. M. Ok, Y. Porter and P. S. Halasyamani, *Chem. Mater.*, 2006, **18**, 2070–2074.
8 S. L. Pan, Y. C. Wu, P. Z. Fu, G. C. Zhang, Z. H. Li, C. X. Du and C. T. Chen, *Chem. Mater.*, 2003, **15**, 2218–2221.
9 Z. G. Hu, M. Yoshimura, Y. Mori and T. Sasaki, *J. Cryst. Growth*, 2005, **275**, 232–239.
10 S. C. Wang, N. Ye, W. Li and D. Zhao, *J. Am. Chem. Soc.*, 2010, **132**, 8779–8786.
11 S. L. Pan, J. P. Smit, C. H. Lanier, M. R. Marvel, L. D. Marks and K. R. Poeppelmeier, *Cryst. Growth Des.*, 2007, **7**, 1561–1564.
12 J. Goodey, J. Broussard and P. S. Halasyamani, *Chem. Mater.*, 2002, **14**, 3174–3180.
13 F. Li, X. L. Hou, S. L. Pan and X. A. Wang, *Chem. Mater.*, 2009, **21**, 2846–2850.
14 F. Kong, S. P. Huang, Z. M. Sun, J. G. Mao and W. D. Cheng, *J. Am. Chem. Soc.*, 2006, **128**, 7750–7751.
15 H. Huang, Y. He, Z. Lin, L. Kang and Y. Zhang, *J. Phys. Chem. C*, 2013, **117**(44), 22986–22994; H. W. Huang, L. Liu, S. Jin, W. Yao, Y. Zhang and C. Chen, *J. Am. Chem. Soc.*, 2013, **135**(49), 18319–18322; H. Huang, J. Yao, Z. Lin, X. Wang, R. He, W. Yao, N. Zhai and C. Chen, *Angew. Chem., Int. Ed.*, 2011, **50**, 9141–9144.
16 X. Y. Fan, S. L. Pan, X. L. Hou, X. L. Tian and J. Han, *Cryst. Growth Des.*, 2010, **10**, 252–256.
17 C. T. Chen, L. Bai, Z. Z. Wang and R. K. Li, *J. Cryst. Growth*, 2006, **292**, 169–178.
18 C. T. Chen, Y. C. Wu, A. Jiang, B. C. Wu, G. You, R. K. Li and S. J. Lin, *J. Opt. Soc. Am. B*, 1989, **6**, 616–621.
19 P. S. Halasyamani, *Chem. Mater.*, 2004, **16**, 3586; H. Y. Chang, S. H. Kim, K. M. Ok and P. S. Halasyamani, *J. Am. Chem. Soc.*, 2009, **131**, 6865.

20 B. C. Wu, D. Y. Tang, N. Ye and C. T. Chen, *Opt. Mater.*, 1996, **5**, 105.
21 T. Sasaki, Y. Mori, M. Yoshimura, Y. K. Yap and T. Kamimura, *Mater. Sci. Eng.*, 2000, **30**, 1.
22 Y. Mori, Y. K. Yap, T. Kamimura, M. Yoshimura and T. Sasaki, *Opt. Mater.*, 2002, **19**, 1.
23 T. Kanai, T. Kanda, T. Sekikawa, S. Watanabe, T. Togashi, C. T. Chen, C. Q. Zhang, Z. Y. Xu and J. Y. Wang, *J. Opt. Soc. Am. B*, 2004, **21**, 370.
24 H. Wu, S. Pan, K. R. Poeppelmeier, H. Li, D. Jia, Z. Chen, X. Fan, Y. Yang, J. M. Rondinelli and H. Luo, *J. Am. Chem. Soc.*, 2011, **133**, 7786–7790.
25 H. Han, G. Yin and D. Wickramaratne, *Comput. Mater. Sci.*, 2013, **69**, 81–86.
26 M. Zhang, X. Su, S. Pan, Z. Wang, H. Zhang, Z. Yang, B. Zhang, L. Dong, Y. Wang, F. Zhang and Y. Yang, *J. Phys. Chem. C*, 2014, **118**, 11849–11856.
27 M. Zhang, S.-L. Pan, X.-Y. Fan, Z.-X. Zhou, K. R. Poeppelmeier and Y. Yang, *CrystEngComm*, 2011, **13**, 2899.
28 X. Gong, X. Zhao, Z. Lv, T. Li, J. You and H. Wang, *Comput. Mater. Sci.*, 2014, **83**, 86–91.
29 M. J. Xia, B. Xu and R. K. Li, *J. Cryst. Growth*, 2014, **404**, 65–68.
30 A. G. Al-Ama, E. L. Belokoneva, S. Yu. Stefanovich, O. V. Dimitrova and N. N. Mochenova, *Crystallogr. Rep.*, 2006, **51**, 225–230.
31 H. Wang, L. Kong, X. Zhao, Z. Lv, T. Li, W. W. Ju, J. You and Y. Bai, *Appl. Phys. Lett.*, 2013, **103**, 101902.
32 N. Ye, Q. Chen, B. C. Wu and C. T. Chen, *J. Appl. Phys.*, 1998, **84**, 555–558.
33 M. Abudoureheman, L. Wang, X. Zhang, H. Yu, Z. Yang, C. Lei, J. Han and S. Pan, *Inorg. Chem.*, 2015, **54**, 4138–4142.
34 J. P. Perdew, K. Burke and M. Ernzerhof, *Phys. Rev. Lett.*, 1996, **77**, 3865–3868.
35 P. Blaha, K. Schwarz, G. K. H. Madsen, D. Kvasnicka and J. Luitz, *WIEN2k, An Augmented Plane Wave Plus Local Orbitals Program for Calculating Crystal Properties*, Vienna University of Technology, Austria, 2001.
36 F. Tran and P. Blaha, *Phys. Rev. Lett.*, 2009, **102**, 226401.
37 A. H. Reshak, H. Huang, H. Kamarudin and S. Auluck, *J. Appl. Phys.*, 2015, **117**, 085703.
38 A. H. Reshak, *RSC Adv.*, 2015, **5**, 70992.
39 L. Ma, Z. Xia, V. Atuchin, M. Molokeev, S. Auluck, A. H. Reshak and Q. Liu, *Phys. Chem. Chem. Phys.*, 2015, **17**, 31188.
40 A. H. Reshak, I. V. Kityk and S. Auluck, *J. Phys. Chem. B*, 2010, **114**, 16705–16712.
41 A. H. Reshak, S. Auluck and I. V. Kityk, *J. Solid State Chem.*, 2008, **181**, 789–795.
42 A. H. Reshak, S. Auluck and I. V. Kityk, *J. Phys.: Condens. Matter*, 2008, **20**, 145209.
43 http://www.wien2k.at/reg_user/textbooks/usersguide.pdf.
44 C. Ambrosch-Draxl and J. O. Sofo, *Comput. Phys. Commun.*, 2006, **175**, 1–14.
45 S. Sharma and C. Ambrosch-Draxl, *Phys. Scr., T*, 2004, **109**, 128.
46 J. W. Lekse, M. A. Moreau, K. L. McNerny, J. Yeon, P. S. Halasyamani and J. A. Aitken, *Inorg. Chem.*, 2009, **48**, 7516–7518.
47 J. A. Brant, D. J. Clark, Y. S. Kim, J. I. Jang, J.-H. Zhang and J. A. Aitken, *Chem. Mater.*, 2014, **26**, 3045–3048.
48 C. T. Chen, N. Ye, J. Lin, J. Jiang, W. R. Zeng and B. C. Wu, *Adv. Mater.*, 1999, **11**, 1071–1078.
49 Z. S. Lin, J. Lin, Z. Z. Wang, C. T. Chen and M. H. Lee, *Phys. Rev. B: Condens. Matter Mater. Phys.*, 2000, **62**, 1757–1764.
50 E. D. Palik, *Handbook of Optical Constants of Solids*, Academic Press, New York, 1985.
51 D. R. Penn, *Phys. Rev. [Sect.] B*, 1962, **128**, 2093.
52 H. Huang, Y. He, X. Li, M. Li, C. Zeng, F. Dong, X. Du, T. Zhangd and Y. Zhang, *J. Mater. Chem. A*, 2015, **3**, 24547–24556.
53 H. Huang, Y. He, Z. Lin, L. Kang and Y. Zhang, *J. Phys. Chem. C*, 2013, **117**, 22986–22994.
54 H. Wu, S. Pan, H. Yu, D. Jia, A. Chang, H. Li, F. Zhang and X. Huang, *CrystEngComm*, 2012, **14**, 799.
55 B. Zhang, M.-H. Lee, Z. Yang, Q. Jing, S. Pan, M. Zhang, H. Wu, X. Su and C.-S. Li, *Appl. Phys. Lett.*, 2015, **106**, 031906.
56 C. T. Chen, Y. C. Wu, A. D. Jiang, B. C. Wu, G. M. You, R. K. Li and S. J. Lin, *J. Opt. Soc. Am. B*, 1989, **6**, 616–621.
57 Y. C. Wu, T. Sasaki, S. Nakai, A. Yokotani, H. Tang and C. T. Chen, *Appl. Phys. Lett.*, 1993, **62**, 2614–2615.
58 Y. Zhou, Y. C. Yue, J. N. Wang, F. Yang, X. K. Cheng, D. F. Cui, Q. J. Peng, Z. G. Hu and Z. Y. Xu, *Opt. Express*, 2009, **17**, 20033–20038.
59 Q. Bian, Z. Yang, L. Dong, S. Pan, H. Zhang, H. Wu, H. Yu, W. Zhao and Q. Jing, *J. Phys. Chem. C*, 2014, **118**, 25651–25657.
60 D. A. Kleinman, *Phys. Rev.*, 1962, **126**, 1977.
61 G. J. Chen, Y. C. Wu and P. Z. Fu, *J. Cryst. Growth*, 2006, **292**, 449–453.
62 D. Xue and Z. Zhang, *Appl. Phys. A: Mater. Sci. Process.*, 1999, **68**, 57–61.
63 D. Li, Q. Jing, C. Lei, S. Pan, B. Zhang and Z. Yang, *RSC Adv.*, 2015, **97**, 79882–79887.
64 R. Y. Boyd, *Principles of Nonlinear Optics*, Academic Press, NY, 1982, p. 420.
65 R. W. Boyd, *Nonlinear Opt.*, Academic Press is an imprint of Elsevier, 3rd edn, 2008, ISBN: 978-0-12-369470-6.